Bayesian image segmentation under varying blur with triplet Markov random field

Sonia Ouali, Jean-Baptiste Courbot, Romain Pierron, Olivier Haeberlé

Bayesian image segmentation under varying blur with triplet Markov random field

Sonia Ouali[1], Jean-Baptiste Courbot[1], Romain Pierron[2] and Olivier Haeberlé[1]

[1] IRIMAS, UR UHA 7499, 61 rue Albert Camus, 68200 Mulhouse, France
[2] LVBE, UR UHA 3391, 33 rue de Herrlisheim, 68008 Colmar, France

E-mail: sonia.ouali@uha.fr, jean-baptiste.courbot@uha.fr, romain.pierron@uha.fr and olivier.haeberle@uha.fr

Abstract. In this paper, we place ourselves in the context of the Bayesian framework for image segmentation in the presence of varying blur. The proposed approach is based on Triplet Markov Random Fields (TMRF). This method takes into account, during segmentation, peculiarities of an image such as noise, blur, and texture. We present an unsupervised TMRF method, which jointly deals with the problem of segmentation, and that of depth estimation in order to process fluorescence microscopy images. In addition to the estimation of the depth maps using the Metropolis-Hasting and the Stochastic Parameter Estimation (SPE) algorithms, we also estimate the model parameters using the SPE algorithm. We compare our TMRF method to other MRF models on simulated images, and to an unsupervised method from the state of art on real fluorescence microscopy images. Our method offers improved results, especially when blur is important.

Keywords: Markov random fields, image segmentation, deconvolution, fluorescence microscopy

1. Introduction

1.1. Context

Probabilistic methods have experienced great success in the context of image segmentation since the publication of the work of Geman and Geman [1]. They are used to solve many problems in machine learning, inverse problems, pattern recognition, and image analysis being that of interest in this paper.

Markov Random Field (MRF) models are a statistical class of models for inference in images. A vast amount of published works using these models can be found, with applications including image restoration [2], edge detection [3], reconstruction [4], and segmentation [5], the problem of interest in this contribution. It consists in partitioning an image formed by a finite set of pixels $\mathcal{S}$ into k non-overlapping regions with $k = |\Omega|$ and $\Omega = \{\omega_1, \omega_2, ..., \omega_k\}$ is the set of values. Let us consider $s \in \mathcal{S}$ a pixel and N_s the neighborhood of s. We consider $\mathbf{X} \in \Omega^{|\mathcal{S}|}$ a vector of random variables defined on $\mathcal{S}$. Then, $\mathbf{X}$ has a MRF distribution if and only if the conditional probability of realization of $\mathbf{x}$ on a site s depends only on realizations of $\mathbf{x}$ within its neighborhood N_s:

$$p(x_s|\mathbf{x}_{\mathcal{S}\setminus s}) = p(x_s|\mathbf{x}_{N_s}) \tag{1}$$

This ability to describe local properties makes MRF useful for image processing because regions in real-life images are often homogeneous in the sense that neighboring pixels tend to have similar properties, such as intensity, color, and texture.

Throughout this work, we consider fluorescence microscopy images. Fluorescent microscopy is a technique that uses fluorescence to generate an image and visualize structures within biological specimens. However, measurements in fluorescence microscopy are affected by blur that acts as a convolution of the object of interest with the microscope's Point Spread Function (PSF). The PSF describes how a point source of light is represented in the image and is a fundamental characteristic of the optical system. This blurring effect can obscure fine details and reduce the overall clarity of the image, making it more challenging to accurately analyze the structures of interest.

We can distinguish two different causes of blur: *depth defocus blur*, when the observed sample is not in the focal plane, and *shake blur*, when the lens or an object in the scene moves during the acquisition. In our microscopy observation conditions, the latter can be neglected, but not the former, as we have no guarantee that the observed sample is exclusively in the focal plane. Defocus blur is partially known because the PSF is known at the instrumental level, (see Fig. 1). For later processing of fluorescence microscopy images, one can experimentally measure the PSF, using sub-resolution fluorescent beads, acquiring their images through the optical system. The interested reader will find in Ref. [6] detailed explanation and protocol to perform this task. This ensures that the actual microscope characteristics are measured, but the procedure can be tedious, and measured PSFs can be noisy. An improvement therefore consists in denoising the experimental PSF [7, 8], or fitting a Gaussian model [9], or a computed PSF to the measured one

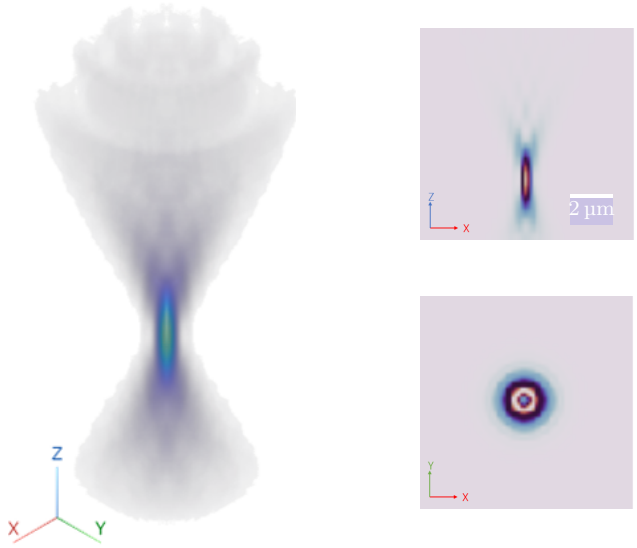

Figure 1: Typical PSF $\mathbf{h}^{3D}$ in fluorescence microscopy generated via PSF generator [14], with axial and longitudinal slices of the central plans. The PSF in fluorescence microscopy is non-homogeneous, aberrations clearly appear in the xz view inducing asymmetry along the optical z-axis, but are less visible in the xy view.

[10]. Finally, if acquisition parameters are well known, the PSF can be computed using scalar [11] or vectorial [12, 13] models of image formation, depending on the required accuracy. In this work, as the microscope characteristics and acquisition parameters are known, we use, for its accuracy and ease of use, the model of Kirshner *et al.* [14], as implemented in the software PSFGenerator [15]. However, the depth at which the sample is located remains unknown, and it must therefore be estimated at each site s in the image. Thus, it is necessary to jointly address the problem of non-stationary deconvolution and segmentation.

1.2. Problem statement

We consider that the blurred and noisy observation image $\mathbf{y}$ is the result of a convolution of a hidden field $\mathbf{z}$, representing the intensity classes, with the instrument PSF $\mathbf{H}$. Since $\mathbf{H}$ is variable according to the region of the image, we parameterize it by a second hidden field $\mathbf{v}$, so that the model writes as:

$$\mathbf{y} = \mathbf{H}(\mathbf{v})\mathbf{z} + \mathbf{n}, \tag{2}$$

where $\mathbf{n}$ is an independent Gaussian noise. The covariance of $\mathbf{n}$ is $\mathbf{\Sigma}_{\mathbf{n}} \in \mathbb{R}^{B\times B\times|\Omega|}$, since we decided to define a covariance per class. The observation $\mathbf{y} \in \mathbb{R}^{S\times B}$ is a colored image with $S = |\mathcal{S}|$ pixels and B colors, *e.g.* $B = 3$ in the case of RGB images. $\mathbf{z} \in \mathbb{R}^{S\times B}$ results from a realization of a MRF $\mathbf{x} \in \Omega^S$. The latter represents the different classes in the image while $\mathbf{z}$ represent their colors, so $\forall s, x_s = \omega_k \iff \mathbf{z}_s = \boldsymbol{\mu}_k$, and $\boldsymbol{\mu}_k \in \mathbb{R}^B$. In

other words, $\mathbf{z}$ corresponds to the noiseless and blur-less version of the observation. We will discuss in detail different MRF models in Section 2.

The operator $\mathbf{H}(\mathbf{v}) \in \mathbb{R}^{S\times S}$ translates the fact that the convolution varies in the image as a function of the latent field $\mathbf{v} \in \mathbb{R}^S$. In each site s in the image, we define it $\forall s \in \mathcal{S}$ as:

$$(\mathbf{H}(\mathbf{v})\mathbf{z})_s = \left\langle \mathbf{h}^{\text{3D}}_{s,v_s}, \mathbf{z} \right\rangle \tag{3}$$

$\mathbf{h}^{\text{3D}} \in \mathbb{R}^{S\times S\times P}$ is known only on a 3D grid, see Fig. 1. P represents the depth of the PSF, $\mathbf{h}^{\text{3D}}_{s,v_s} \in \mathbb{R}^S$ represents the PSF of the system at depth v_s in the site s. In other words, $\mathbf{H}$ forms a depth-selection operator to model the blur. It is also important to note that the field $\mathbf{v}$ does not necessarily have a physical interpretation, its sole purpose is to parameterize the 3D PSF.

1.3. Related work

Popular approaches to solving segmentation problems include clustering-based methods [16, 17], graph-based methods [18], or Bayesian methods [19, 20, 21, 22, 23]. A lot of works used Bayesian methods to solve complex segmentation problems when dealing with noisy and blurred [24], textured [25], or even fluorescence images [26]. In recent works with a related formulation, one can cite [24], in which the authors proposed a pairwise MRF model allowing for the unsupervised Bayesian segmentation of faint sources in astronomical hyperspectral images, known to be blurry and noisy. Authors in [27] also presented a probabilistic model called Gaussian Pairwise Markov Random Field (GPMRF), for images corrupted by long-range spatially correlated noise.

In addition to segmentation, deconvolution is a necessary step when dealing with blurry images. Several studies developed methods for image deconvolution or segmentation/deconvolution purposes. For instance, authors in [28] present a deconvolution method based on Gaussian and non-Gaussian MRF prior. A method for deconvolution-segmentation of textured images is given in [29]. This method relies on a hierarchical model and a Bayesian strategy to jointly estimate the labels, the texture, and the hyperparameters. Other deconvolution methods are applied to fluorescence microscopy images in which the fluorescent points are perceived as a blur. The authors in [30, 31, 32, 33] propose deconvolution methods applied to different types of real images: ultrasound, scanner, and others. In [34] the author proposes a deconvolution method based on MRF. The PSF is considered spatially invariant, as in [35] where the PSF intervenes within a model of pairwise MRF. The authors in [36] have on the other hand considered that the PSF is spatially variant, which is more realistic for actual microscopy images. Indeed, as previously stated, in fluorescence microscopy, blur varies with depth [37]. To be able to work with a continuous PSF, the authors in [26] consider a constant per area PSF. These methods have been proven effective on simulated and real images. Although the authors conclude that their methods can just as easily be applied to microscopy images, their algorithms do not take into consideration the peculiarities of these kinds of images. The blur in fluorescence microscopy images is often much

more important than the one we can see in macroscopic ones. Besides, none of the cited methods has been tested on actual fluorescence images.

We seek a method that takes into account the depth-varying PSF, and that does both deconvolution to return a blur map and segmentation to return the labels. We also seek unsupervised segmentation since we do not have a database of grapevine images, so we need to estimate the parameters.

In this paper, we present a method that makes it possible to jointly estimate $\mathbf{x}$, $\mathbf{v}$, and the parameters of the model, from the sole knowledge of $\mathbf{y}$ and $\mathbf{h}^{3D}$. First, we discuss the different MRF models and their applications (Section 2). Then, we discuss the joint deconvolution/segmentation method we developed with the parameter estimation (Section 2.3 and 3), and we finish by presenting the results we obtained.

Note that in this article, we use the terms convolution and deconvolution in order to qualify kernel-varying convolution and deconvolution. This variation in the window (kernel) represents the slices of the PSF. For the annotations, Roman letters refer to random variables, while bold letters refer to random vectors. $\mathbf{x}$ is a realization of the random field $\mathbf{X}$, and for simplification, when there is no ambiguity, we will write $p(\mathbf{X} = \mathbf{x}) = p(\mathbf{x})$, and the same annotation will be used for the other random vectors.

2. Models

In this section, we discuss different levels of complexity of MRF models within a Bayesian framework. The simplest and yet efficient model used in literature is the Hidden Markov Random Field (HMRF). Pairwise Markov Random Fields (PMRF) were introduced in the case where the hidden class field is not necessarily Markovian [25], so one assumes the couple (class field $\mathbf{X}$, observation field $\mathbf{Y}$) is Markovian. The latter-described models may fail in the case of a non-stationary process. To tackle this problem, Triplet Markov Random Fields (TMRF) were introduced [38]. They are formulated by adding an auxiliary random field to the class and observation ones so that the three together ($\mathbf{X}$, $\mathbf{Y}$, $\mathbf{V}$) are considered as Markovian.

2.1. Hidden Markov Random Field

In HMRF, one makes two assumptions. The first one is about the class field $\mathbf{X}$, one assumes that $\mathbf{X}$ has a Markov field distribution that can be modeled with a Gibbs representation:

$$p(\mathbf{x}) = \gamma \exp(-U(\mathbf{x})), \tag{4}$$

with:

$$U(\mathbf{x}) = \sum_{e \in E} \psi_e(\mathbf{x}_e), \tag{5}$$

where γ is a normalization constant, sometimes called the partition function, ψ is a potential function, and E is the pixel sets of cliques on the image. In this work, we consider cliques of size 2. The most popular examples of such models used in literature

are the Ising model and the Potts model (used here). We consider the MRF $\mathbf{X}$ taking values in Ω^S. The law of $\mathbf{x}$ is written as:

$$p(\mathbf{x}) = \exp\left(-\alpha \sum_{(s,t)\in E} \Big(1 - 2\delta(x_s, x_t)\Big)\right), \tag{6}$$

with $\alpha > 0$ the parameter modulating the granularity of $\mathbf{x}$, and δ the Kronecker symbol. In the following, without loss of generality, $\mathbf{x}$ will have values in two classes $\Omega = \{\omega_0, \omega_1\}$, which means that $k = 2$. Indeed, this corresponds to the application on real images (see Section 4.3).

The second classical HMRF assumption is about the observation $\mathbf{y}$. We assume an independent noise so the probability of the observed data is obtained as:

$$p(\mathbf{y}|\mathbf{x}) \propto \prod_{s\in\mathcal{S}} p(\mathbf{y}_s|x_s) \tag{7}$$

In the case of Gaussian white noise with a class covariance $\mathbf{\Sigma}_{\mathbf{n},k} \in \mathbb{R}^{B\times B}$ and color $\boldsymbol{\mu}_k \in \mathbb{R}^B$ (k represents the classes in the image):

$$p(\mathbf{y}_s|x_s = \omega_k) \sim \mathcal{N}(\mathbf{y}_s; \boldsymbol{\mu}_k, \mathbf{\Sigma}_{\mathbf{n},k}) \tag{8}$$

By taking into account Eqs. (6)(8), the law of the HMRF model is rewritten as:

$$\begin{aligned} p(\mathbf{x}, \mathbf{y}) &= p(\mathbf{x}) \prod_{s\in\mathcal{S}} p(\mathbf{y}_s|x_s) \\ &\propto \exp\left(-\alpha \sum_{(s,t)\in E} \Big(1 - 2\delta(x_s, x_t)\Big)\right) \\ &\times \prod_{s\in\mathcal{S}} \exp\left(-\frac{1}{2}(\mathbf{y}_s - \boldsymbol{\mu}_k)^T \mathbf{\Sigma}^{-1}_{\mathbf{n},k_s}(\mathbf{y}_s - \boldsymbol{\mu}_k)\right) \end{aligned} \tag{9}$$

where $k_s \in \Omega$ is the class of x_s. We can represent the HMRF with a dependence graph, as in Fig. 2 (a). In this model, the set of parameters is $\mathbf{\Theta}_{\text{HMRF}} = \{\alpha, \mathbf{\Sigma}_{\mathbf{n},0}, \mathbf{\Sigma}_{\mathbf{n},1}, \boldsymbol{\mu}_0, \boldsymbol{\mu}_1\}$.

2.2. Pairwise Markov Random Field

The estimation of $\mathbf{X} = \mathbf{x}$ from $\mathbf{Y} = \mathbf{y}$ requires the knowledge of the posterior distribution $p(\mathbf{x}|\mathbf{y})$, which is easily available in the HMRF case. This is in fact possible if we assume that the couple $(\mathbf{X}, \mathbf{Y})$ has a Markov field distribution. In this case, we call $(\mathbf{X}, \mathbf{Y})$ a PMRF [25]. It is different from a HMRF since $\mathbf{X}$ is not necessarily Markovian, and neither $\mathbf{Y}$.

Considering an independent noise and a blurry image with an invariant PSF $\mathbf{h}^{\text{2D}} \in \mathbb{R}^{S\times S}$, we can write:

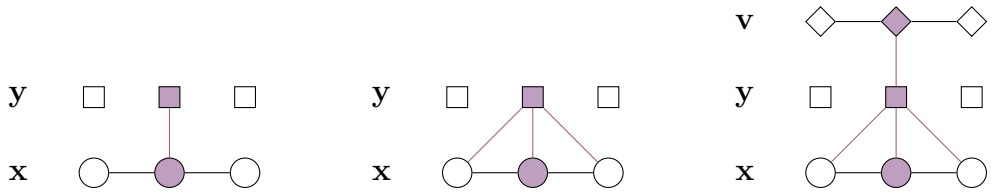

(a) HMRF (b) PMRF (c) TMRF

Figure 2: Dependency graph of the three MRF models used in this paper, conditionally to a site s (colored). The absence of link between two variables means that they are independent given the variables in the s site. Note that for clarity, only one dimension of the lattice is represented.

$$\begin{aligned} p(\mathbf{y}|\mathbf{x}) &= \prod_{s\in\mathcal{S}} p(\mathbf{y}_s|\mathbf{x}) \\ &= \prod_{s\in\mathcal{S}} \exp\left(-\frac{1}{2}\left(\mathbf{y}_s - [\mathbf{h}^{\mathrm{2D}}\mathbf{z}]_s\right)^T \boldsymbol{\Sigma}_{\mathbf{n},k_s}^{-1}\left(\mathbf{y}_s - [\mathbf{h}^{\mathrm{2D}}\mathbf{z}]_s\right)\right) \end{aligned} \tag{10}$$

Then, taking into account Eqs. (6)(10), the law of the PMRF model is given by:

$$\begin{aligned} p(\mathbf{x},\mathbf{y}) &\propto p(\mathbf{x}) \prod_{s\in\mathcal{S}} p(\mathbf{y}_s|\mathbf{x}) \\ &= \exp\left(-\alpha \sum_{(s,t)\in E}\Big(1-2\delta(x_s,x_t)\Big)\right) \\ &\times \prod_{s\in\mathcal{S}} \exp\left(-\frac{1}{2}\left(\mathbf{y}_s - [\mathbf{h}^{\mathrm{2D}}\mathbf{z}]_s\right)^T \boldsymbol{\Sigma}_{\mathbf{n},k_s}^{-1}\left(\mathbf{y}_s - [\mathbf{h}^{\mathrm{2D}}\mathbf{z}]_s\right)\right) \end{aligned} \tag{11}$$

The set of parameters in this case is the same as in HMRF as $\mathbf{h}^{\mathrm{2D}}$ is known, so $\boldsymbol{\Theta}_{\mathrm{PMRF}} = \{\alpha, \boldsymbol{\Sigma}_{\mathbf{n},0}, \boldsymbol{\Sigma}_{\mathbf{n},1}, \boldsymbol{\mu}_0, \boldsymbol{\mu}_1\}$.

2.3. Triplet Markov Random Field

In TMRF, a third process $\mathbf{V}$ is introduced, and the triplet $(\mathbf{X}, \mathbf{Y}, \mathbf{V})$ is assumed to be Markovian. TMRF makes it possible to more efficiently work with non-stationary images, and possibly deal with non-Gaussian correlated noise [39]. Generally speaking, the field $\mathbf{V}$ might have or not have a physical interpretation, so it can be used to describe latent phenomena with no direct interpretation in the image; it could be used to define different homogeneities of $(\mathbf{X}, \mathbf{Y})$, such as the possible non-stationarity of the distribution $p(\mathbf{x}, \mathbf{y})$, as it could also be used to model textures. To our knowledge, in previous works mentioning TMRF, $\mathbf{V}$ is always discretely valued. In this work, we assume $\mathbf{V} \in \mathbb{R}^S$, and it represents the depths of the observed points with respect to the PSF, as introduced in

the observation model (Eqs. (2) (3)). We choose to simplify the Markov distribution of TMRF as follows:

$$p(\mathbf{x}, \mathbf{y}, \mathbf{v}) \propto p(\mathbf{y}|\mathbf{x}, \mathbf{v})p(\mathbf{x}, \mathbf{v}) \tag{12}$$

By choosing $\mathbf{x}$ and $\mathbf{v}$ independents:

$$p(\mathbf{x}, \mathbf{y}, \mathbf{v}) \propto p(\mathbf{y}|\mathbf{x}, \mathbf{v})p(\mathbf{x})p(\mathbf{v}) \tag{13}$$

The distribution of $\mathbf{y}$ conditionally to $\mathbf{x}$ and $\mathbf{v}$ can be written as:

$$p(\mathbf{y}|\mathbf{x}, \mathbf{v}) \propto \exp\left(-\frac{1}{2}\Big(\mathbf{y} - \mathbf{H}(\mathbf{v})\mathbf{z}\Big)^T \mathbf{\Sigma}_{\mathbf{n},k_s}^{-1}\Big(\mathbf{y} - \mathbf{H}(\mathbf{v})\mathbf{z}\Big)\right) \tag{14}$$

The dependency graph corresponding to a TMRF is shown in Fig. 2 (c).

We work with PSF $\mathbf{h}^{\mathrm{3D}}$ as described in Eq. (3). We assume that $\mathbf{v}$ is a realization of a zero-mean Gaussian Markov random field:

$$p(\mathbf{v}) \propto \exp\left(-\frac{1}{2}\mathbf{v}^T\mathbf{\Sigma}^{-1}\mathbf{v}\right) \tag{15}$$

We assume that $\mathbf{\Sigma} \in \mathbb{R}^{S\times S}$ is a circulant covariance matrix, whose basis is parameterized by a Gaussian correlation function r. This means, for any pair of pixels $(\boldsymbol{i}, \boldsymbol{j})$ in the image:

$$\mathbf{\Sigma}_{\boldsymbol{i},\boldsymbol{j}} = \sigma_{\mathbf{v}}^2 r(\boldsymbol{i}, \boldsymbol{j}; \rho) = \sigma_{\mathbf{v}}^2 \exp\left(-\frac{1}{\rho^2}\left\|\boldsymbol{i} - \boldsymbol{j}\right\|_t^2\right) \tag{16}$$

where $\sigma_{\mathbf{v}}$ is the standard deviation, ρ the range of typical correlations between pixels, and $\left\|\boldsymbol{i} - \boldsymbol{j}\right\|_t$ represents the distance on the torus between sites $\boldsymbol{i}$ and $\boldsymbol{j}$. We consider an image defined on a torus: the left edge connects to the right edge, and the top edge connects to the bottom edge. We will also note the precision matrix $\mathbf{Q} = \mathbf{\Sigma}^{-1}$. $\mathbf{Q}$ and $\mathbf{\Sigma}$ are circulant matrices, so they are characterized by their bases, denoted $\mathbf{b_Q} \in \mathbb{R}$ and $\mathbf{b_\Sigma} \in \mathbb{R}$ respectively. The calculation of the base in the Fourier domain is sufficient in this work, instead of the calculation and the storage of the matrix $\mathbf{\Sigma}$ or $\mathbf{Q}$. In practice, the base $\mathbf{b_Q}$ can be calculated as follow:

$$\mathbf{b_Q} = \mathrm{IDFT}(1 \div \mathrm{DFT}(\mathbf{b_\Sigma})) \tag{17}$$

$$\mathbf{xQ} = \mathrm{IDFT}(\mathrm{DFT}(\mathbf{x}) \otimes \mathrm{DFT}(\mathbf{b_Q})) = \mathbf{x} * \mathbf{b_Q} \tag{18}$$

Where DFT is the Discrete Fourier Transform, and IDFT its inverse; $\div$ and $\otimes$ are element-by-element division and multiplication, respectively, so there is no need to handle $\mathbf{Q}$ or $\mathbf{\Sigma}$ entirely.

Finally, taking into account Eqs. (6)(14)(15), the law of the TMRF model we introduce is expressed as:

$$
\begin{aligned}
p(\mathbf{T}) &\propto p(\mathbf{x}) \prod_{s\in\mathcal{S}} p(\mathbf{y}_s|\mathbf{x},\mathbf{v})p(\mathbf{v}) \\
&= \exp\left(-\alpha \sum_{(s,t)\in E} \Big(1-2\delta(x_s,x_t)\Big)\right) \\
&\times \prod_{s\in\mathcal{S}} \exp\left(-\frac{1}{2}\Big(\mathbf{y}_s-[\mathbf{H}(\mathbf{v})\mathbf{z}]_s\Big)^T \boldsymbol{\Sigma}_{\mathbf{n},k_s}^{-1}\Big(\mathbf{y}_s-[\mathbf{H}(\mathbf{v})\mathbf{z}]_s\Big)\right) \\
&\times \exp\left(-\frac{1}{2}\mathbf{v}^T\boldsymbol{\Sigma}^{-1}\mathbf{v}\right),
\end{aligned} \tag{19}
$$

all the parameters of the model being gathered in $\boldsymbol{\Theta} = \{\boldsymbol{\Sigma}_{\mathbf{n},0}, \boldsymbol{\Sigma}_{\mathbf{n},1}, \boldsymbol{\mu}_0, \boldsymbol{\mu}_1, \alpha, \rho, \sigma_v\}$. Since we are in the context of unsupervised segmentation, $\boldsymbol{\Theta}$ has to be estimated. We will discuss in the next section the different Bayesian estimation methods we consider in this work.

3. Bayesian Inference

In this section, we show how to estimate $\mathbf{x}$ in the context of Eq. (19) from the observation $\mathbf{y}$ and $\mathbf{h}^{3D}$, and without knowing neither $\mathbf{v}$ nor $\boldsymbol{\Theta}$. For this, we first study how to estimate each element of $(\mathbf{x}, \mathbf{v}, \boldsymbol{\Theta})$ when $\mathbf{y}$ and the other two vectors are known, in order to afterward design an alternating algorithm.

3.1. Estimation of $\mathbf{x}$

By fixing $\mathbf{v}$ and $\boldsymbol{\Theta}$, we find ourselves in the context of supervised segmentation within the framework of PMRF, which takes into account a blur, here fixed prior to estimation [24]. For this, we resort to Bayesian estimators. Bayes law and the Markovian properties of $\mathbf{X}$ in PMRF, of $(\mathbf{X}, \mathbf{Y})$ in PMRF, and of $(\mathbf{X}, \mathbf{Y}, \mathbf{V})$ in TMRF allow us to use different Bayesian estimators methods as the *Maximum A Posteriori (MAP)*:

$$
\hat{x}_s^{\mathrm{MAP}} = \arg\max_{\boldsymbol{\omega}\in\Omega} p_{\boldsymbol{\Theta}}(\mathbf{x}=\boldsymbol{\omega}|\mathbf{y}), \tag{20}
$$

or the *Marginal Posterior Mode (MPM):*

$$
\forall s \in \mathcal{S} : \hat{x}_s^{\mathrm{MPM}} = \arg\max_{\omega\in\Omega} p_{\boldsymbol{\Theta}}(x_s=\omega|\mathbf{y}), \tag{21}
$$

The MAP estimator can be approached using the *Iterative Conditional Mode* (ICM) algorithm introduced in [40]. This algorithm is known for its ease of implementation and efficiency. Authors in [41] presented an algorithm for approximating the MPM estimator. The latter uses the Gibbs sampler [1] to generate a number of estimations of $\hat{\mathbf{x}}$. MPM estimator is time-consuming and gives in preliminary experiments a similar estimation of $\mathbf{x}$ as in the MAP estimator. We therefore decide in the following to focus only on the MAP estimator.

3.2. Estimation of $\mathbf{v}$

Finding an estimator for $\mathbf{v}$ similar to MAP/MPM estimators is not easy, because $\mathbf{v}$ does not intervene linearly in the image model (Eq. (2) (14)). However, if we consider that $\mathbf{x}$ and $\boldsymbol{\Theta}$ are fixed, the posterior $p_{\boldsymbol{\Theta}}(\mathbf{v}|\mathbf{x}, \boldsymbol{\Theta})$ is accessible via the likelihood (Eq. (2)) and the prior on $\mathbf{v}$ (Eq. (15)), so we can write:

$$p_{\boldsymbol{\Theta}}(\mathbf{v}|\mathbf{x}, \mathbf{y}) \propto p(\mathbf{y}|\mathbf{x}, \mathbf{v})p(\mathbf{v}) \tag{22}$$

To estimate $\mathbf{v}$, we use the Metropolis-Hastings (MH) algorithm [42], which iteratively allows for making proposals on $\mathbf{v}$, to evaluate their posterior distributions, and to either retain them or not. The main steps of the MH algorithm are reported in the following:

(i) At a step t of the MH algorithm, the proposal made is a disturbance of the current state $\mathbf{v}^{(t)}$:

$$\mathbf{v}^{\text{proposal}} = \mathbf{v}^{(t)} + \epsilon \mathbf{v}^{\text{disturbance}}, \tag{23}$$

where $\mathbf{v}^{\text{disturbance}}$ sampled from a multivariate normal law $\mathcal{N}(0, \boldsymbol{\Sigma}_{\mathbf{v}})$, with the same parameters as $\mathbf{v}$ (Eq. (15)), and where $\epsilon > 0$ defines the amplitude of the disturbance.

(ii) Then the proposal is accepted with probability:

$$\min\left(1, \frac{p_{\boldsymbol{\Theta}}(\mathbf{v}^{\text{proposal}}|\mathbf{x}, \mathbf{y})}{p_{\boldsymbol{\Theta}}(\mathbf{v}^{(t)}|\mathbf{x}, \mathbf{y})}\right). \tag{24}$$

If the proposal is not accepted, then $\mathbf{v}^{(t+1)} = \mathbf{v}^{(t)}$.

The whole, sufficiently repeated, forms a Markov chain whose stationary state provides:

$$\mathbf{v}^{\text{MH}} \sim p_{\boldsymbol{\Theta}}(\mathbf{v}|\mathbf{x}, \mathbf{y}) \tag{25}$$

Various Markov Chain Monte Carlo (MCMC) methods exist in the context of sampling complex distributions. Examples include Metropolis-adjusted Langevin algorithms, Hamiltonian Monte Carlo, and Hamiltonian-assisted Metropolis sampling [43]. These methods exploit the gradient information in the target density (see Eq. (22)). However, this is not applicable in our case because $\mathbf{v}$ acts as a depth selection operator within a discrete object, the PSF. Therefore, we work with the simpler MH algorithm.

3.3. Estimation of $\boldsymbol{\Theta}$

In unsupervised segmentation, each model parameter must be estimated. Note that we assume here that $\mathbf{x}$, $\mathbf{v}$, and $\mathbf{y}$ are known.

Mean and variance estimation. *The Maximum Likelihood Estimator* (MLE) is used to estimate the parameters of the normal distributions, namely $\boldsymbol{\mu}_0$, $\boldsymbol{\mu}_1$, σ_v, $\boldsymbol{\Sigma}_{\mathbf{n},0}$, and $\boldsymbol{\Sigma}_{\mathbf{n},1}$.

Granularity coefficient estimation. In works involving the Potts model, the granularity parameter is either fixed or estimated. There exists no MLE for the estimation of α. A Pseudo MLE does exist [44]. An improvement of this method for Potts MRF model parameter estimation is presented in [45]. It approaches α as follow:

$$\hat{\alpha} = \frac{k^2}{2(k-1)}(F_{\text{neq}} - \frac{1}{k}) \tag{26}$$

with k the number of classes in the image, and F_{neq} representing the frequency of neighbor pairs of different classes:

$$F_{\text{neq}} = \frac{1}{k} \sum_{(s,t)\in E} \delta(x_s, x_t) \tag{27}$$

Our choice for estimating α in the context of segmentation is the Pseudo MLE method, which is easy to implement yet provides sufficient accuracy.

Correlation estimation. To our knowledge, there exists no MLE for ρ, so we will use a Least Squares (LS) method as in [46]. It allows for fitting a Gaussian function to the correlogram $\mathcal{C}(d)$ of $\mathbf{v}$, d (between 0 and N) being the distance on the torus of a pair of pixels. The LS estimator yields:

$$\hat{\rho} = ((\mathbf{E}^T\mathbf{E})^{-1}\mathbf{E}^T\mathbf{w})^{-1} \tag{28}$$

with $\mathbf{w^T} = (\log\hat{\mathcal{C}}(0), ..., \log\hat{\mathcal{C}}(N))$ and $\mathbf{E^T} = (0, ..., N)$ a vector of $N+1$ elements.

The correlogram $\hat{\mathcal{C}}$ of the zero-mean field $\mathbf{v}$ for a distance d can be estimated by:

$$\hat{\mathcal{C}}(d) = \frac{1}{|\mathcal{D}(d)|} \sum_{(s,s')\in\mathcal{D}(d)} \frac{1}{\hat{\sigma^2_{\mathbf{v}}}} v_s v_{s'} \tag{29}$$

where $\mathcal{D}(d)$ is the set of pixel pairs whose Manhattan distance on torus is d:

$$\mathcal{D}(d) = \{(s,s') \in \mathcal{S}^2 : ||s - s'||_t = d\} \tag{30}$$

3.4. Unsupervised segmentation

In the context of unsupervised segmentation, we only possess the observation $\mathbf{y}$. We are therefore interested in the joint estimation of $\mathbf{x}$, $\mathbf{v}$, and $\mathbf{\Theta}$ from the observation $\mathbf{y}$ and the knowledge of $\mathbf{h}^{3D}$. A popular method, in this case, is *Expectation-Maximization* (EM) proposed in [47]. Its algorithm cycles between computing the expectation of $\mathbf{x}$ and maximizing the complete data log-likelihood to obtain the MLE of $\mathbf{\Theta}$. EM has proven convergence properties, but there is no guarantee to find the global maxima [48]. Its stochastic variant (SEM) [49] is a viable alternative. This algorithm incorporates a stochastic step, which simulates a realization of $\mathbf{x}^t$ based on the current estimate $\mathbf{\Theta}^t$. The addition of this step makes it possible to not remain stuck at local minima, unlike conventional EM. Many articles compare EM and SEM, [48, 50, 51, 52]. All agree that

SEM is the least computationally demanding, may display faster convergence, as well as improves the ability to locate the global maximum of the likelihood function.

These methods consider exclusively MLE, which is not the case for the estimation of the parameters ρ (Eq. (28)) and α (Eq. (26)). We also need to estimate the field $\mathbf{v}$, which we consider as a necessary parameter to find $\mathbf{x}$. Here we provide a method based on the SEM algorithm, which we call Stochastic Parameter Estimation (SPE) as in [27]. The latest will return the estimated parameters $\boldsymbol{\Theta}$ and $\mathbf{v}$ that we will use in a MAP estimator to find $\mathbf{x}$ (Eq. (20)). The procedure is described in Algorithm 1. The field $\mathbf{v}$ is initialized randomly. The class field $\mathbf{x}$ is set up using the k-means algorithm [53] on the observation $\mathbf{y}$. The mean and covariance parameters in $\boldsymbol{\Theta}$ can be initialized randomly or for a gain of time, using a quasi-SEM algorithm on the initialized fields $\mathbf{x}$ and $\mathbf{v}$. To summarize, our method consists in:

- From $\mathbf{y}$ and $\mathbf{H}$, we estimate $\hat{\boldsymbol{\Theta}}$ and $\hat{\mathbf{v}}$ (SPE in algorithm 1).
- From $\mathbf{y}$, $\hat{\boldsymbol{\Theta}}$ and $\hat{\mathbf{v}}$, we estimate $\hat{\mathbf{x}}$ (ICM [40]).

Algorithm 1 Stochastic Parameter Estimation (SPE) procedure

Require: $\mathbf{y}$, $\mathbf{H}$.
Ensure: $\hat{\mathbf{v}}$, $\hat{\boldsymbol{\Theta}} = \{\hat{\boldsymbol{\Sigma}}_{\mathbf{n}}, \hat{\sigma}_{\mathbf{v}}, \hat{\boldsymbol{\mu}}, \hat{\alpha}, \hat{\rho}\}$.
1. Initialisation: give initial configurations for $\mathbf{x}^{(0)}$, $\mathbf{v}^{(0)}$ and values for $\boldsymbol{\Theta}^{(0)}$.
repeat (iteration $t+1$):
2. Simulate $\mathbf{x}^{(t+1)} \sim p_{\boldsymbol{\Theta}^{(t)}}(\mathbf{x}|\mathbf{y}, \mathbf{v}^{(t)})$ by running a Gibbs sampler for t iterations.
3. Simulate $\mathbf{v}^{(t+1)} \sim p_{\boldsymbol{\Theta}^{(t)}}(\mathbf{v}|\mathbf{y}, \mathbf{x}^{(t+1)})$. (25)
4. Estimate $\boldsymbol{\Theta}^{(t+1)}$ from $\mathbf{y}, \mathbf{x}^{(t+1)}, \mathbf{v}^{(t+1)}$ using :
- MLE estimator for $\boldsymbol{\Sigma}_{\mathbf{n}}$, $\sigma_{\mathbf{v}}$, $\boldsymbol{\mu}_0$ and $\boldsymbol{\mu}_1$.
- Pseudo MLE for α. (26)
- LS estimator for ρ. (28)
until Stability of $\hat{\boldsymbol{\Theta}}$.

The SPE algorithm is stochastic, so it does not converge pointwise. Thus, in practice, we stop it when the result $\hat{\boldsymbol{\Theta}}^t$ of the last iteration deviates sufficiently little (less than 5%) from the average of the previous 10 iterations.

4. Numerical Results

This section gathers the performances of the model we propose. First, we review in detail the algorithmic considerations for the practical implementation of SPE. Then, we evaluate the models from Section 2 under varying blur and Signal to Noise Ratio (SNR). Finally, we test our TMRF model on real images and compare the result to those obtained from another filtering method from the literature, discussed in detail in Section 4.3.

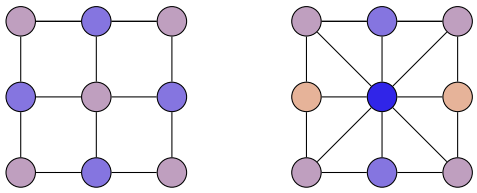

(a) 4-neighbors (b) 8-neighbors

Figure 3: Two colored model and four colored model on sets $\mathcal{S}$ containing 3×3 sites of the chromatic Gibbs sampler. Each circle represents a site and each color is a subdivision of $\mathcal{S}$.

4.1. Algorithmic consideration

Chromatic sampling. The estimation of $\mathbf{x}$ (Eq. (20)) requires the use of a Gibbs sampler [1], a popular MCMC algorithm used to simulate samples from the joint distribution. The Gibbs sampler is constructed by sequentially sampling each variable in the model:

- Select a prior $p(\mathbf{x} = k)$ from $k = |\Omega|$.
- Construct conditional given the neighborhood N_s^G.
- Update the variable.

N_s^G is the neighborhood considered in the Gibbs sampling. The Gibbs sampler is ergodic and easy to implement, but time-consuming. Authors in [54] have proposed a method to accelerate Gibbs sampling, called the chromatic Gibbs sampler. It applies the graph coloring technique in order to obtain a direct parallelization of the classic sequential scan Gibbs sampler. To work with the chromatic sampler, we need to ensure that only independent variables are sampled simultaneously; the neighborhood of a pixel must not be sampled while sampling that particular pixel. To do so, the PSF must be ignored outside the disk of radius r (see Fig. 4). To determine in practice, the best radius r, we change r beyond which the PSF is ignored and run our algorithm on synthetic images. We also test the case where the previously mentioned condition is not respected, by fixing the size of the neighborhood $N_s^G = N_s$ and vary r.

The results are reported in Fig. 5. The error rate is calculated by dividing the number of misclassified pixels by the total number of pixels in the image. As one can see in Fig. 5(a), the higher the value of the radius, the smaller the error, because by choosing a higher value of r, we keep most of the information in the PSF. We can also see by comparing the two graphs, MAP with varying neighborhood N_s^G and MAP with fixed neighborhood $N_s^G = N_s$, that the difference between the two methods is very small for low values of r ($\approx 1\%$). This difference is slightly higher for higher values of r ($\approx 4\%$). Now, if we look at the time a segmentation takes, see Fig. 5(b), this error is compensated by an important gain of time when working with the MAP with a fixed neighborhood. This method allows us to take larger values of r and do the segmentation in a shorter time.

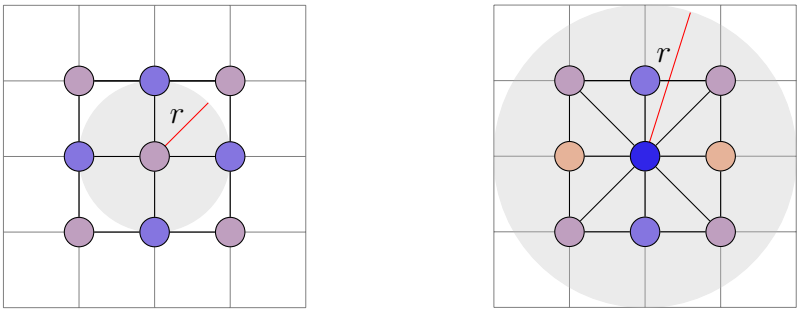

Figure 4: Two examples of neighborhoods N_s in the left and N_s^G in the right, with their corresponding truncated PSF in the case of the chromatic sampler.

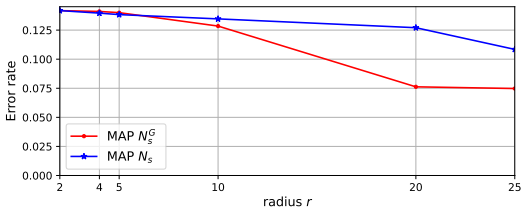

(a) Summary of the error rates obtained as a function of the radius r of the PSF

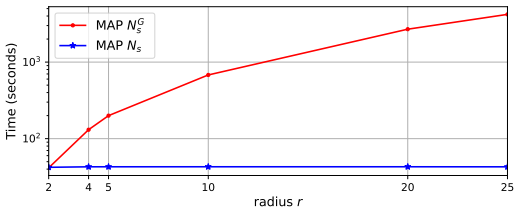

(b) Summary of the time obtained as a function of the radius r of the PSF. Note that the time curves here are in logarithmic scale.

Figure 5: (a) Error rates and (b) time as a function of the radius r estimated by 100 different realizations. The graph is obtained by running the algorithm with images of size 100×100 pixels.

In this article, we use the principle of the chromatic sampler to implement the ICM algorithm, from which all the results are obtained, with a time gain factor of 1000 with respect to the classical sequential sampler.

PSF discretization. The PSF we consider in our model is numerically discretized, so a discrete version of the Gaussian field $\mathbf{v}$ (see Fig 6a) is used during the selection of depths. We want to find the best value of τ that gives a good compromise between precision and cost. To do so, we vary the values of τ and run the algorithm on synthetic images and for different values of the radius. From the results presented in Fig. 7, we deduce that the smaller the value of τ the more precise the segmentation. The higher the value of τ, the faster the segmentation, but the higher the error. Our goal is to choose the smallest value of the error in the function of the step and the radius. This corresponds to choosing $r = 20$ and $\tau = 2$.

MH disturbance amplitude ϵ In Eq.(23), ϵ defines the amplitude of the disturbance for the proposals made in MH. A low value will produce a high acceptance rate, but low-risk taking, and therefore a slow convergence; conversely, a value that is too high

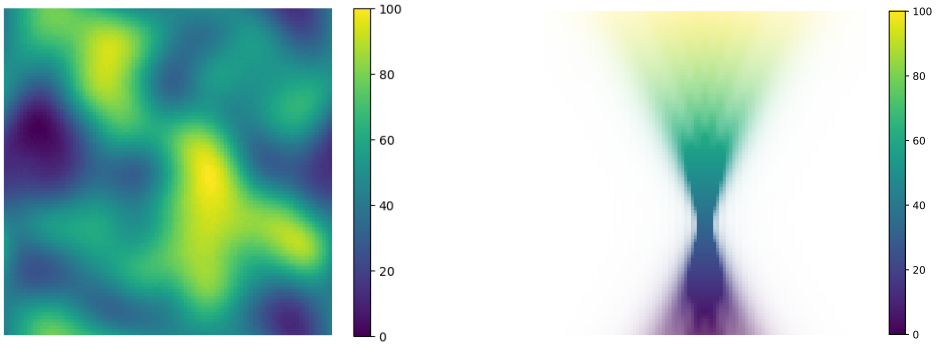

(a) (b)

Figure 6: Gaussian field used to represent blur. The yellow color corresponds to the regions affected with the upper half of the PSF, the green and blue-green colors correspond to those affected with the middle part of the PSF, while the dark blue and purple colors correspond to regions affected with the lower half part.

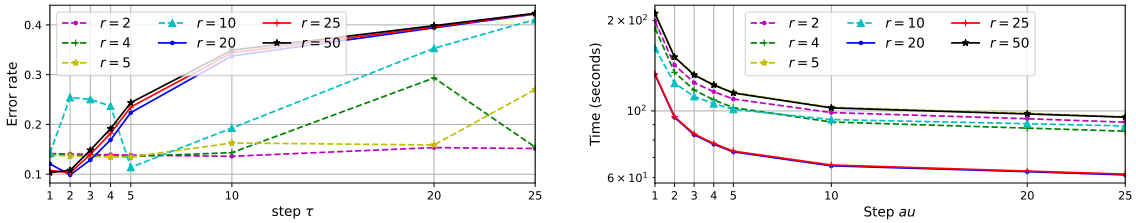

(a) Error rates obtained as a function of τ and for different values of r.

(b) Time obtained as a function of τ and for different values of r. Note that the curves are in logarithmic scale.

Figure 7: (a) Error rates and (b) time as a function of the step τ estimated by 100 different realizations. The graph is obtained by running the algorithm with images of size 100×100 pixels.

can produce propositions too implausible to be accepted. Sometimes, when the nature of the target distribution is known, an optimal value of ϵ is proposed, as in the case of a Gaussian posterior distribution of dimension D for which $\epsilon = 2.38/\sqrt{D}$ [55]. This is not applicable to our case because the posterior $p_{\mathbf{\Theta}}(\mathbf{v}|\mathbf{x}, \mathbf{y})$ (cf Eq 22) is not Gaussian since there is a discretization that intervenes in Eq. (3). We therefore take a value of ϵ, which empirically gives the best compromise between acceptance rate and risk-taking. This value is fixed for all experiments $\epsilon = 20$ and modifies only the computation speed.

4.2. Results on synthetic images

In this part, we test using synthetic images the different above-cited models, HMRF, PMRF, and TMRF. Microscopy images are noisy and blurry, so to test the models, at first, we will vary the Signal to Noise Ratio (SNR), to test them on different noisy

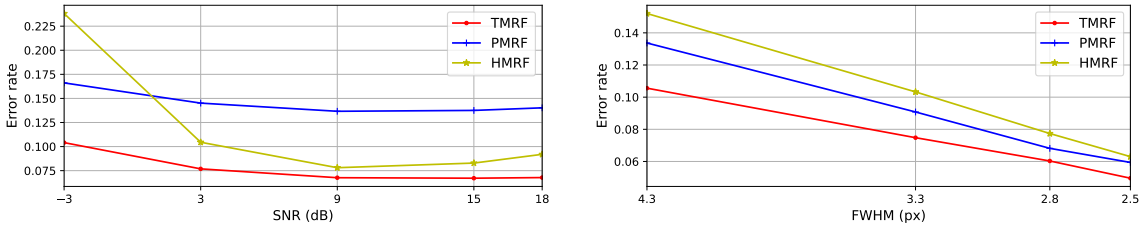

(a) Error rates obtained as a function of SNR. (b) Error rates obtained as a function of FWHM.

Figure 8: Summary of the experiment on synthetic images. The graphs were obtained by running the algorithms with images of size 100 × 100 pixels. Each point corresponds to the average of 100 different realizations.

images. Then, we will vary the PSF Full With at Half Maximum (FWHM), in order to test them on different blurry images. The SNR used was defined as follows:

$$\mathrm{SNR} = 10 \log_{10} \left(\frac{\|\mathbf{Hx}\|^2}{\sigma_{\mathbf{n}} S} \right) \tag{31}$$

All the algorithms are unsupervised. Results are shown in Figs. 8(a) and 8(b).

As one can see from Fig. 8(a), our TMRF achieved better results compared with the HMRF and PMRF for all values of the SNR. One can also remark that from SNR=3 dB, the HMRF achieves better results than the PMRF. This can be interpreted by the fact that the PSF considered in PMRF is invariant, which is not true in reality, so we can say that it is better not to take into consideration the PSF when using HMRF than using a wrong PSF in PMRF. Remark that in the case of very noisy images (SNR=-3dB) the PMRF performs better than HMRF. One can also remark from the three graphs, that the less noisy the image, the better the result, as expected.

We also varied the FWHM of the PSF. The larger the FWHM, the blurrier the image. The results of the three methods are shown in Fig. 8(b). The first remark is that the three curves are decreasing, meaning that for all methods, the less blurry the image, the better the result, again as expected. One can also remark that our TMRF achieves better results compared to the PMRF which achieves in turn better results than the HMRF. The latter is not intended to deal with blur. We can deduce from the curves that, fully taking into account a 3D PSF and a possibility of variations is better than a 2D and invariant one on varying blur images. Segmenting an image of size 100 x 100 using the TMRF model takes approximately 15 minutes using a standard laptop. The code used in this article will be made publicly available on `https://github.com/courbot/BISUVAB-TMF` upon acceptance of this manuscript

4.3. Fluorescence microscopy images

In this section, we test our model on real microscopy images. We work on fluorescence microscopy grapevine wood images (cf. Fig. 9) infected with the esca-associated fungus

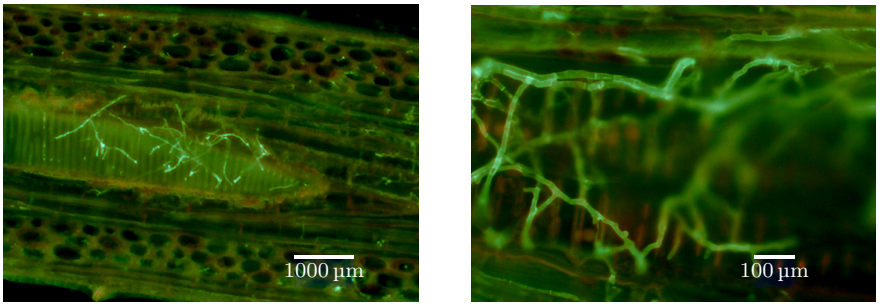

Figure 9: Examples of pathogen in vine wood images observed with a fluorescence microscope, at x10 magnification on the left and x40 on the right. The pathogen fluorescence appears as green-yellow filaments, while wood auto-fluorescence appears as yellow-brown.

Neofusiccicum parvum. Esca is a wood disease causing early plant decline [56]. We specifically focus on the problem of segmentation of the pathogen in the wood. This fungal, which was colored using WGA-FITC dye appears with a light green fluorescent color and has a filamentary texture, while the wood exhibits auto-fluorescence and is very textured, contrary to the pathogen. The images are noisy, textured, and have blurry areas, which makes them difficult to segment. The images are obtained using a wide-field BX51 Olympus microscope with a laser excitation at 480 nm, and an ORCA-Fusion Hamamatsu CMOS camera.

4.3.1. Acquisition protocol. R.P, a researcher at LVBE and a grapevine-microbe interaction expert, was in charge of making the images. He inoculated one-year-old potted Gewurztraminer cuttings with fungal mycelium, cut the 25 µm thick slices using a microtome, and observed them in the microscope after a WGA-fitc staining treatment according to [57]. We ended with a small bank of vinewood images. He also provided us with the ground truth images that he obtained by manually segmenting each image. As in this case, we don't have the real ground truth, we use the expert segmentation as ground truth, which means there could be some room for error. All the coming segmentations are done on x40 magnification images, so they have the same scale as the left one in Fig. 9.

4.3.2. Alternatives. In [58], the authors present a filtering method dealing with the segmentation of 2D curvilinear structures. They test their method on retinal and crack images, finding good results, especially on crack images that have a really noisy background. Since our microscopy images do present filiform structures and a textured background, we compare our work to the one presented in this article. The method is called RORPO (Ranking the Orientation Responses of Path Operators). It uses the principle of path operators and tends to avoid false detections that other local analysis methods may produce. RORPO returns two features, a *directional feature* that provides local orientation and an *intensity feature* that can be seen as a curvilinearity measure.

In this work, we are interested by the latter feature. RORPO returns images in gray level. To be able to compare with our binary resulting images, we converted the obtained RORPO images binary images using the mean threshold.

4.3.3. Results. In Fig. 10, we show some segmentation results using the three studied HMRF, PMRF, and TMRF models, and the RORPO method. These methods are able to detect the filamentary mycelium in wood. Differences mainly appear in the blurry areas and areas where the texture of the wood is really visible (vessels and cells). Several comments can be made:

- In the first image, the pathogen grew outside the wood. There, no textured background is visible, which makes the segmentation task easier, and both RORPO and the Markov models give good results.
- In the second image, the pathogen is located inside a vessel. The latter has a filamentary structure and a frequency similar to the one of the pathogen. The RORPO, HMRF, and PMRF methods detect the pathogen and some parts of the vessel (autofluorescence), while TMRF could make the difference between the two. It is also the case in the third image where RORPO and the HMRF detect wood and pathogen, while TMRF detects only the pathogen. The PMRF failed to segment this image.
- The structure of the pathogen appears differently depending on the woodcut, which can be transverse or lateral. The fourth image is a transverse cut: the pathogen doesn't appear filamentary anymore. The TMRF method gives good segmentation results, which in this configuration is not the case for the three other methods.
- The last image was obtained from a different microscope and a different camera. Since we do not have detailed information about this material, we work with the same theoretical PSF as used for the other images. We can see that this image is blurry. The RORPO, HMRF, and PMRF methods do not detect any pathogen in the blurry areas. The TMRF detects all the pathogens even in the blurry part of the image.
- In addition to the segmentation, TMRF returns a depth map $\hat{\mathbf{v}}$. $\hat{\mathbf{v}}$ estimates that the yellow and dark blue regions represent the blurry areas, hence areas where segmentation is difficult. Whereas the light green regions represent the focal plane.

5. Conclusion and perspectives

In this paper, we presented a TMRF model considering the problems of segmentation and non-stationary deconvolution of an image. We detailed how parameter estimation and joint kernel varying deconvolution and segmentation are made possible within the proposed model. Simulations and experiments concerning the segmentation quality were also introduced and showed the model to be relevant to the considered problem, and more efficient than its HMRF and TMRF counterparts. The model has also been tested

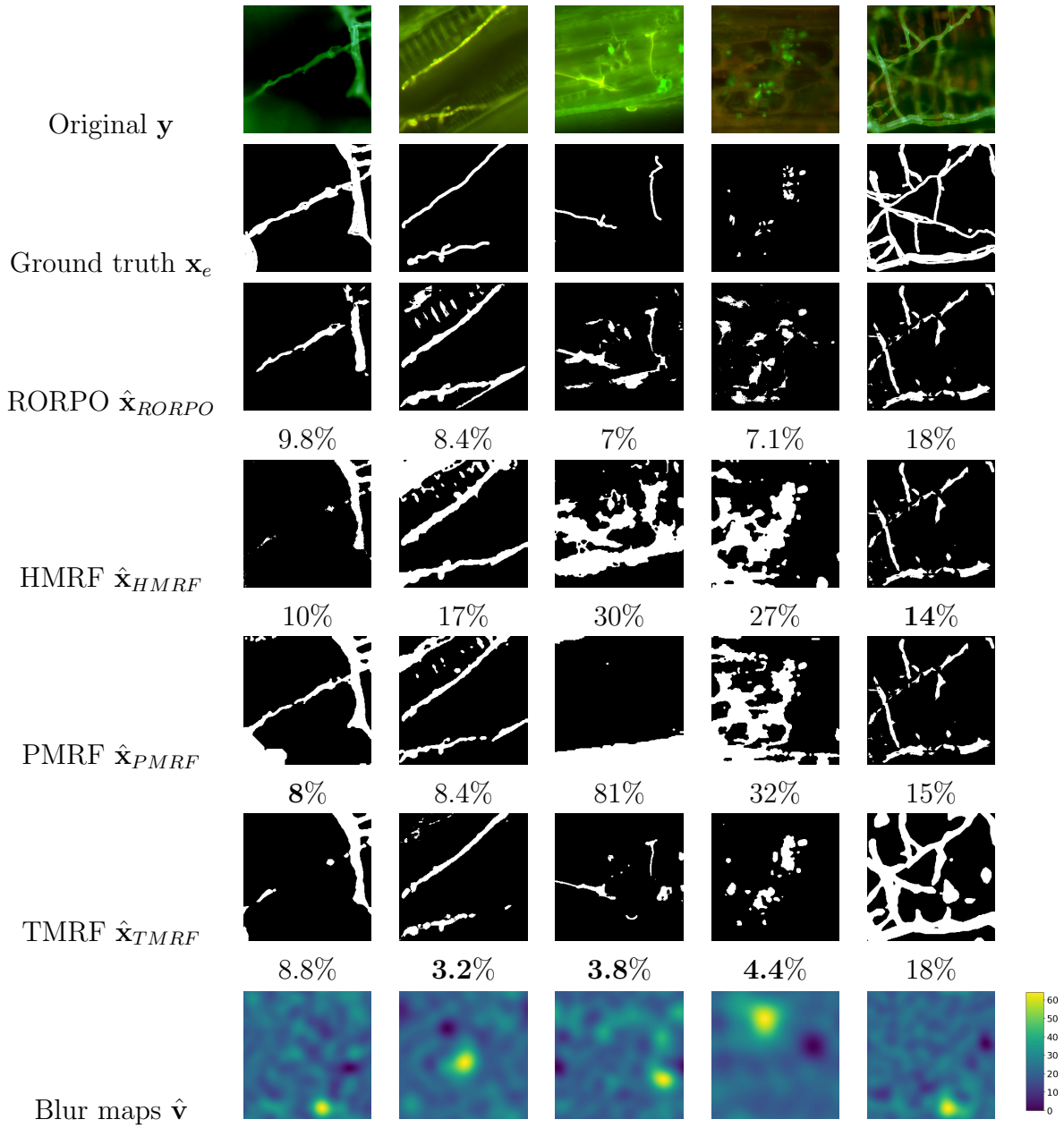

Figure 10: Segmentation results on vine wood fluorescence microscopy images with associated blur maps. The best error rate for each image is shown in bold

on real images, and a comparison with a state-of-the-art method was introduced. The algorithm behavior yields satisfactory results for our needs.

Future works could focus on the possible algorithmic developments from this model. We could also consider the use of a Gaussian field for the simulation of $\mathbf{x}$ instead of a Markov field. Finally, considering the blind deconvolution to estimate the PSF of the system could also be of interest.

Acknowledgments

We are grateful to UEAV, INRAE, 2023, doi: 10.15454/1.5483269027345498E12. Viticulture Facility, for providing us with grapevine material.

References

[1] Geman S and Geman D 1984 Stochastic relaxation, Gibbs distributions, and the Bayesian restoration of images *IEEE Transactions on Pattern Analysis and Machine Intelligence* **PAMI-6** 721–741

[2] Chen Y, Pock T, Ranftl R and Bischof H 2013 Revisiting loss-specific training of filter-based MRFs for image restoration *Pattern Recognition: 35th German Conference, GCPR 2013, Saarbrücken, Germany, September 3-6, 2013. Proceedings 35* (Springer) pp 271–281

[3] Ferraioli G 2010 Multichannel in SAR building edge detection *IEEE Transactions on Geoscience and Remote Sensing* **48** 1224–1231

[4] Mehta B B, Ma D, Pierre E Y, Jiang Y, Coppo S and Griswold M A 2018 Image reconstruction algorithm for motion insensitive MR Fingerprinting (MRF): MORF *Magnetic Resonance in Medicine* **80** 2485–2500

[5] Pham T X, Siarry P and Oulhadj H 2020 Segmentation of MR brain images through hidden Markov random field and hybrid metaheuristic algorithm *IEEE Transactions on Image Processing* **29** 6507–6522

[6] Cole R W, Jinadasa T and Brown C M 2011 Measuring and interpreting point spread functions to determine confocal microscope resolution and ensure quality control *Nature protocols* **6** 1929–1941

[7] Lai X, Lin Z, Ward E and Ober R J 2005 Noise suppression of point spread functions and its influence on deconvolution of three-dimensional fluorescence microscopy image sets *Journal of microscopy* **217** 93–108

[8] Maalouf E, Colicchio B and Dieterlen A 2011 Fluorescence microscopy three-dimensional depth variant point spread function interpolation using zernike moments *JOSA A* **28** 1864–1870

[9] Stallinga S and Rieger B 2010 Accuracy of the gaussian point spread function model in 2d localization microscopy *Optics express* **18** 24461–24476

[10] Haeberlé O, Bicha F, Simler C, Dieterlen A, Xu C, Colicchio B, Jacquey S and Gramain M P 2001 Identification of acquisition parameters from the point spread function of a fluorescence microscope *Optics communications* **196** 109–117

[11] Gibson S F and Lanni F 1991 Experimental test of an analytical model of aberration in an oil-immersion objective lens used in three-dimensional light microscopy *JOSA A* **8** 1601–1613

[12] Haeberlé O 2003 Focusing of light through a stratified medium: a practical approach for computing microscope point spread functions. part i: Conventional microscopy *Optics communications* **216** 55–63

[13] Haeberlé O 2004 Focusing of light through a stratified medium: a practical approach for computing microscope point spread functions: Part ii: confocal and multiphoton microscopy *Optics communications* **235** 1–10

[14] Kirshner H, Aguet F, Sage D and Unser M 2013 3-D PSF fitting for fluorescence microscopy: implementation and localization application *Journal of Microscopy* **249** 13–25

[15] Kirshner H and Sage D 2019 Psf generator https://bigwww.epfl.ch/algorithms/psfgenerator/

[16] Arthur D and Vassilvitskii S 2007 K-means++: The advantages of careful seeding *Proceedings of the Eighteenth Annual ACM-SIAM Symposium on Discrete Algorithms* SODA '07 (Society for Industrial and Applied Mathematics) p 1027–1035 ISBN 9780898716245

[17] Luo M, Ma Y F and Zhang H J 2003 A spatial constrained K-means approach to image segmentation *Fourth International Conference on Information, Communications and Signal Processing, 2003 and the Fourth Pacific Rim Conference on Multimedia. Proceedings of the 2003 Joint* vol 2 (IEEE) pp 738–742

[18] Peng B, Zhang L and Zhang D 2013 A survey of graph theoretical approaches to image segmentation *Pattern Recognition* **46** 1020–1038 ISSN 0031-3203

[19] Bouman C A and Shapiro M 1994 A multiscale random field model for Bayesian image segmentation *IEEE Transactions on Image Processing* **3** 162–177

[20] Orbanz P and Buhmann J M 2008 Nonparametric Bayesian image segmentation *International Journal of Computer Vision* **77** 25–45

[21] D'Elia C, Poggi G and Scarpa G 2003 A tree-structured Markov random field model for Bayesian image segmentation *IEEE Transactions on Image Processing* **12** 1259–1273

[22] Kwon Y, Won J H, Kim B J and Paik M C 2020 Uncertainty quantification using Bayesian neural networks in classification: Application to biomedical image segmentation *Computational Statistics & Data Analysis* **142** 106816

[23] Xiao Z, Adel M and Bourennane S 2013 Bayesian method with spatial constraint for retinal vessel segmentation *Computational and Mathematical Methods in Medicine* **2013**

[24] Courbot J B, Mazet V, Monfrini E and Collet C 2019 Pairwise Markov fields for segmentation in astronomical hyperspectral images *Signal Processing* **163** 41–48

[25] Pieczynski W and Tebbache A N 2000 Pairwise Markov random fields and segmentation of textured images *Machine Graphics and Vision* **9** 705–718

[26] Hadj S B, Blanc-Féraud L, Aubert G and Engler G 2013 Blind restoration of confocal microscopy images in presence of a depth-variant blur and Poisson noise *2013 IEEE International Conference on Acoustics, Speech and Signal Processing* (IEEE) pp 915–919

[27] Gangloff H, Courbot J B, Monfrini E and Collet C 2021 Unsupervised image segmentation with Gaussian pairwise Markov fields *Computational Statistics & Data Analysis* **158** 107178

[28] Courbot J B and Colicchio B 2022 Transformed Gaussian random fields for unsupervised image deconvolution *IEEE Signal Processing Letters* **29** 2702–2706

[29] Giovannelli J F and Vacar C 2017 Deconvolution-segmentation for textured images *2017 25th European Signal Processing Conference (EUSIPCO)* (IEEE) pp 191–195

[30] Yuan L, Sun J, Quan L and Shum H Y 2008 Progressive inter-scale and intra-scale non-blind image deconvolution *ACM Transactions on Graphics (TOG)* **27** 1–10

[31] Zhao N, Basarab A, Kouamé D and Tourneret J Y 2016 Joint segmentation and deconvolution of ultrasound images using a hierarchical Bayesian model based on generalized Gaussian priors *IEEE Transactions on Image Processing* **25** 3736–3750

[32] Krishnan D and Fergus R 2009 Fast image deconvolution using hyper-Laplacian priors *Advances in Neural Information Processing Systems* **22**

[33] Xu L, Ren J S, Liu C and Jia J 2014 Deep convolutional neural network for image deconvolution *Advances in Neural Information Processing Systems* **27**

[34] Mignotte M 2006 A segmentation-based regularization term for image deconvolution *IEEE Transactions on Image Processing* **15** 1973–1984

[35] Courbot J B and Mazet V 2021 Pairwise and hidden Markov random fields in image segmentation *2020 28th European Signal Processing Conference (EUSIPCO)* (IEEE) pp 2458–2462

[36] Preza C and Conchello J A 2004 Depth-variant maximum-likelihood restoration for three-dimensional fluorescence microscopy *Journal of the Optical Society of America A* **21** 1593–1601

[37] Maalouf E 2010 *Contribution to fluorescence microscopy, 3D thick samples deconvolution and depth-variant PSF* Ph.D. thesis Université de Haute Alsace-Mulhouse

[38] Benboudjema D and Pieczynski W 2005 Unsupervised image segmentation using triplet Markov fields *Computer Vision and Image Understanding* **99** 476–498

[39] Benboudjema D and Pieczynski W 2007 Unsupervised statistical segmentation of nonstationary images using triplet Markov fields *IEEE Transactions on Pattern Analysis and Machine Intelligence* **29** 1367–1378

[40] Besag J 1986 On the statistical analysis of dirty pictures *Journal of the Royal Statistical Society: Series B (Methodological)* **48** 259–279

[41] Marroquin J, Mitter S and Poggio T 1987 Probabilistic solution of ill-posed problems in

computational vision *Journal of the American Statistical Association* **82** 76–89

[42] Gelman A, Carlin J B, Stern H S and Rubin D B 1995 *Bayesian data analysis* (Chapman and Hall/CRC)

[43] Song Z and Tan Z 2021 Hamiltonian-assisted metropolis sampling *Journal of the American Statistical Association* 1–19

[44] Ali A M, Farag A A and Gimel'farb G 2008 Analytical method for MGRF Potts model parameter estimation *2008 19th International Conference on Pattern Recognition* (IEEE) pp 1–4

[45] Levada A L, Mascarenhas N D and Tannús A 2008 Pseudolikelihood equations for Potts MRF model parameter estimation on higher order neighborhood systems *IEEE Geoscience and Remote Sensing Letters* **5** 522–526

[46] Cressie N 2015 *Statistics for spatial data* (John Wiley & Sons)

[47] Dempster A P, Laird N M and Rubin D B 1977 Maximum likelihood from incomplete data via the EM algorithm *Journal of the Royal Statistical Society: Series B (Methodological)* **39** 1–22

[48] Dias J G and Wedel M 2004 An empirical comparison of EM, SEM and MCMC performance for problematic Gaussian mixture likelihoods *Statistics and Computing* **14** 323–332

[49] Celeux G, Chauveau D and Diebolt J 1996 Stochastic versions of the EM algorithm: an experimental study in the mixture case *Journal of statistical computation and simulation* **55** 287–314

[50] Blömer J, Bujna K and Kuntze D 2014 A theoretical and experimental comparison of the EM and SEM algorithm *2014 22nd International Conference on Pattern Recognition* (IEEE) pp 1419–1424

[51] Faria S and Soromenho G 2012 Comparison of EM and SEM algorithms in Poisson regression models: a simulation study *Communications in Statistics-Simulation and Computation* **41** 497–509

[52] Novais L and Faria S 2021 Comparison of the EM, CEM and SEM algorithms in the estimation of finite mixtures of linear mixed models: a simulation study *Computational Statistics* **36** 2507–2533

[53] Lloyd S P 1982 Least squares quantization in pcm *IEEE Transactions on Information Theory* **28** 129–137

[54] Gonzalez J, Low Y, Gretton A and Guestrin C 2011 Parallel Gibbs sampling: From colored fields to thin junction trees *Proceedings of the Fourteenth International Conference on Artificial Intelligence and Statistics* (JMLR Workshop and Conference Proceedings) pp 324–332

[55] Roberts G O and Rosenthal J S 2001 Optimal scaling for various Metropolis-Hastings algorithms *Statistical science* **16** 351–367

[56] Pierron R *et al.* 2015 Deciphering the niches of colonisation of vitis vinifera L. by the esca-associated fungus phaeoacremonium aleophilum using a GFP marked strain and cutting systems *PLoS One* **10** e0126851

[57] Carotenuto G and Genre A 2020 Fluorescent staining of arbuscular mycorrhizal structures using wheat germ agglutinin (wga) and propidium iodide *Arbuscular Mycorrhizal Fungi: Methods and Protocols* 53–59

[58] Merveille O, Naegel B, Talbot H, Najman L and Passat N 2017 2D filtering of curvilinear structures by ranking the orientation responses of path operators (RORPO) *Image Processing On Line* **7** 246–261